Title
Analytical thermo-mechanics 3D model of friction pendulum bearings

Journal
Earthquake Engineering & Structural Dynamics, 45(6)

ISSN
0098-8847

Authors
Monti, Giorgio
Petrone, Floriana

Publication Date
2016-05-01

DOI
10.1002/eqe.2693

Peer reviewed

Analytical thermo-mechanics 3D model of friction pendulum bearings

Giorgio Monti[1,2] and Floriana Petrone[3,*,†]

[1] Department of Structural and Geotechnical Engineering, Sapienza University of Rome, 00197, Rome, Italy [2] 1-k Scholar, College of Civil Engineering, Hunan University, 410082, Changsha, China [3] Energy Geosciences Division, Lawrence Berkeley National Laboratory, 1 Cyclotron Road, Berkeley, CA 94720, USA

*Correspondence to: Floriana Petrone, Postdoctoral Research Associate, Energy Geosciences Division, Lawrence Berkeley National Laboratory, 1 Cyclotron Road, Berkeley, CA 94720, USA.

[†] E-mail: FlorianaPetrone@lbl.gov; petrone@ucdavis.edu

Summary

Among the most effective seismic protection devices, friction pendulum (FP), whose conceptual basis lies in the pendulum motion and its simple analytical description, has now gained a widespread acceptance. All the studies carried out so far have explored almost all the remarkable features of this device. Among the most appealing are constant stiffness, constant oscillation period, and recentering capability. These studies – and the authors found no exception – have systematically made reference to the classical gravity pendulum equation, whose motion occurs only in one dimension (1D), according to one DOF: the polar angle θ. When the presence of bi-directional seismic excitation required a 2D model, authors have resorted to the vector combination of the response of two orthogonal 1D pendulums, which we refer to as '1.5D' pendulum. Actually, FP is more correctly described as a 2D spherical pendulum, consisting of a mass moving on a sphere with friction, according to two DOFs: the polar angle θ and the azimuth angle ϕ. The relevant analytical equations of motion are presented in this paper, also accounting for thermo-mechanical coupling, to model the friction-induced temperature on the contact surface. The so-developed equations have been the object of an ample parametric study. This has allowed to observe some – sometimes notable – features in the FP response, both in free oscillation state and under bi-directional or tri-directional earthquake-like action, which in some cases lead to a different response with respect to what is generally computed – and designed – under the simplified assumptions of 1D or '1.5D' pendulum motion.

KEY WORDS: thermo-mechanics 3D model; friction pendulum motion equations; tri-directional earthquake excitation; dynamic stiffness

1 Introduction

Friction pendulum (FP) bearings are passive sliding recentering devices whose behavior is based on the principle of pendulum motion [1]. They consist of a concave surface and a pad that slides on it with controlled friction. The

pad moves only when the shear force across the isolation interface overcomes the static friction force and, once the motion starts, the pad moves along the surface, causing the supported mass to follow the surface geometry. The first pioneering studies were carried out on single FPs [2-4] and served to justify that the classical one-dimensional (1D) pendulum equation could describe well the system response by using a single DOF, the polar angle θ. It was then ascertained that the dynamic characteristics of FP bearings depend on two parameters: the (constant) radius of curvature R of the concave surface and the friction coefficient μ of the contacting materials [5].

Once found that the classical 1D pendulum was able to describe the response of the FP with sufficient accuracy, most of the initial researches focused on what was considered to be the most critical parameter in determining the FP dynamic response: the friction coefficient μ, which was more difficult to control than the radius R. Constantinou *et al*. [6] developed a mathematical model for Teflon sliding pads where μ was made to depend on the sliding velocity and the axial pressure. This study took advantage of an extensive testing campaign on FPs subjected to unidirectional loading, presented in a work by Mokha *et al*. [7]. Subsequently, Mokha *et al*. [8] carried out one of the few examples of tests with bi-directional motion currently available in the literature. The focus of that study, rather than trying to identify some peculiar aspects of the FP motion in 2D, was primarily that of checking the validity of the previously calibrated friction models.

In later studies, many authors [9, 10] pointed out that FPs' motion is a function of not only the sphere radius but of the axial load as well. In those cases where the vertical component of the ground motion is relevant, such as in near-field earthquakes with pulse-like motions, this quantity changes and so does the motion. Almazan *et al*. [11] conducted a numerical study on FP bearings under multiple ground motion components with an in-depth analysis of the influence of the vertical components on the FP response. In that study it is proved that variations in normal contact forces, large deformations and uplift, even though not considerably affecting the global system response, have to be considered in modeling and design of FP bearings. This is true especially for near-field earthquakes, where the resulting instantaneous increase in normal force, due to overturning and vertical impact, makes the slider to stop from sliding and to transmit significantly larger shear forces to the supported columns.

A further investigation on the effect of tri-directional ground motions on the force-displacement response was conducted by Mosqueda *et al*. [12], underlining the importance of modeling FPs with two horizontal input components and with a variable vertical load for an accurate determination of the forces transmitted by the bearings to the superstructure.

These works are among the few with a tentative to explicitly account for the 2D behavior of the FP. However, in both of them, this was achieved through

a simple vector combination of the independent responses of two orthogonal 1D FPs, one oscillating along x and the other along y. For the sake of conciseness, we will refer to these models as '1.5D' models.

Starting from the mentioned studies, the authors have found that most of the works developed in the following period have never questioned the classical 1D pendulum equation approach. The combination of two orthogonal 1D pendulums, although being an oversimplifying assumption, results in a highly appealing property for a FP. In fact, when the friction coefficient is low, the oscillation period can be well approximated by that of the frictionless pendulum, which depends only on the spherical surface radius R and is therefore constant. Because the mass carried by a single FP is also constant, this implies that its stiffness remains constant during the oscillation. In this case, the stiffness is defined as the force along a meridian corresponding to a unit polar angle variation bringing the pad towards the FP bottom at any instant. This definition is true for a 1D pendulum and is of course retained in the '1.5D' pendulum, seen as a combination of two orthogonal 1D pendulums with equal and constant stiffness. However, this is certainly inappropriate for describing a 2D motion, where, in addition to the polar angle θ, one should also consider the motion of the pad along the azimuth angle φ. Then, as an extreme example, one may easily conceive a steady motion along a parallel (orbital motion). In this case, the FP becomes a conical pendulum, whose stiffness is of course 0, because the oscillation period towards the bottom is infinite. During an earthquake-induced motion, the pad may actually move along meridians (where the stiffness is constant and well defined as in the '1.5D' FP), but it may certainly move along parallels and along any intermediate trajectory (where the stiffness is lower). This phenomenon is worth investigating, and is exactly the objective of this paper. In fact, in addition to not to be theoretically rigorous, this misinterpreted property of constant stiffness may lead, for example, to the wrong conclusion that an isolation system made of FPs under a building produces a perfect coincidence between center of mass and center of stiffness, thus preventing torsional effects to develop during earthquake motion.

Once the analytical model was developed, it was easily extended to include temperature, which represents a fundamental variable to be checked during the response of a FP, because it affects the friction coefficient [13-19] and therefore the very effectiveness of the isolation system. In this study, temperature is considered as an additional DOF so that, overall, the developed FP model includes three DOFs: θ, ϕ, and T. The inclusion of temperature was inspired by previous studies proving the relationship between temperature and friction coefficients (e.g., [17, 19, 20]). However, to date, the findings of these theoretical and experimental studies have been just applied to '1.5D' models. In this work, it is shown that the same formulations can be easily implemented in the proposed 3D model, but in a more rigorous manner, because temperature is included in the set of

differential equations, giving a complete and rigorous mechanical description of FP bearings. In this initial study, however, the friction coefficient is assumed as constant. Its dependence on temperature will be addressed in ongoing further studies.

After the studies mentioned previously, further research has produced many different FP variants, that is, the double and triple FPs [21, 22]. Although technologically different, they all share the same basic concept of the original one, so the considerations presented in this paper, although developed with reference to the single FP, can be easily extended to its subsequent variants.

The paper concludes with a parametric study to assess the influence of various quantities on the FP response subjected to earthquake-like motion. Particular attention is given to the estimate of the maximum displacement and the stiffness changes occurring during the motion. The former quantity is evaluated as the average over a set of 20 analyses performed with acceleration time histories generated from PSD spectrum. The parameters made to vary within their extremes are: the radius of the sphere, the friction coefficient, the PSD frequency content, and the presence or not of the vertical component of the acceleration, to simulate near-field or far-field earthquake-like motion. It might be worth noticing that the range of values adopted for the friction coefficient is of theoretical interest and that the lowest values are seldom found in practical cases for single FPs. Finally, some comparisons between the overall responses of '1.5D' and 2D pendulums are presented, to better appreciate the time history responses of some fundamental output quantities, such as trajectories and stiffness.

2 Two-Dimensional Analytical Model of a Friction Pendulum

In the following, a 'full' 2D analytical model is developed, representing a point sliding with friction on a concave surface having the shape of a sphere with radius R.

2.1 Lagrange equations of motion

In a spherical coordinate system, the three following Lagrangian coordinates describe the motion in time t of a point P (representing the pad) having mass m:

$$\boldsymbol{q}(t) = [\, q_1(t) \quad q_2(t) \quad q_3(t) \,]^T = [\, r(t) \quad \theta(t) \quad \varphi(t) \,]^T \quad (1)$$

where $r(t) =$ radial distance, $\theta(t) =$ polar angle, and $\phi(t) =$ azimuth angle (Figure 1).

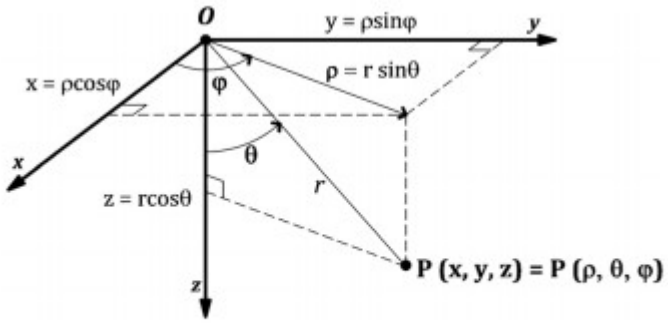

Figure 1. Spherical and Cartesian coordinate systems.

The transformation from spherical to Cartesian (S2C) coordinates and vice versa (C2S) is obtained through the following matrices, respectively,

$$\boldsymbol{S}_{S2C}(t) = \begin{bmatrix} \sin\theta(t)\cos\varphi(t) & \cos\theta(t)\cos\varphi(t) & -\sin\varphi(t) \\ \sin\theta(t)\sin\varphi(t) & \cos\theta(t)\sin\varphi(t) & \cos\varphi(t) \\ \cos\theta(t) & -\sin\theta(t) & 0 \end{bmatrix} \quad (2)$$

$$\boldsymbol{S}_{C2S}(t) = \begin{bmatrix} \sin\theta(t)\cos\varphi(t) & \sin\theta(t)\sin\varphi(t) & \cos\theta(t) \\ \cos\theta(t)\cos\varphi(t) & \cos\theta(t)\sin\varphi(t) & -\sin\theta(t) \\ -\sin\varphi(t) & \cos\varphi(t) & 0 \end{bmatrix} \quad (3)$$

Notice that $S_{S2C}(t) = S_{C2S}(t)^T = S_{C2S}(t)^{-1}$.

If the point is constrained to move on the surface of a sphere having radius R, then $r(t) = R$ and its motion is uniquely identified by the kinematic vectors $p(t)$, $v(t)$, and $a(t)$ describing position, velocity, and acceleration of the constrained point as a function of time, respectively. The kinematic vectors (where each dot denotes a time derivative) are as follows:

$$\boldsymbol{p}(t) = R\boldsymbol{e}_r(t) \quad (4)$$

$$\boldsymbol{v}(t) = R\left(\dot{\theta}(t)\boldsymbol{e}_\theta(t) + \dot{\varphi}(t)\sin\theta(t)\boldsymbol{e}_\varphi(t)\right) \quad (5)$$

$$\boldsymbol{a}(t) = \dot{\boldsymbol{v}}(t) = R\begin{bmatrix} \left(-\dot{\theta}^2(t) - \dot{\varphi}^2(t)\sin^2\theta(t)\right)\boldsymbol{e}_r(t) + \\ +\left(\ddot{\theta}(t) - \dot{\varphi}^2(t)\sin\theta(t)\cos\theta(t)\right)\boldsymbol{e}_\theta(t) + \\ +\left(\ddot{\varphi}(t)\sin\theta(t) + 2\dot{\theta}(t)\dot{\varphi}(t)\cos\theta(t)\right)\boldsymbol{e}_\phi(t) \end{bmatrix} \quad (6)$$

Equations 4, 5, and 6 can be conveniently rewritten in matrix notation as:

$$\boldsymbol{p}(t) = \begin{bmatrix} R \\ 0 \\ 0 \end{bmatrix} \quad (7)$$

$$\boldsymbol{v}(t) = R\begin{bmatrix} 0 \\ \dot{\theta}(t) \\ \dot{\varphi}(t)\sin\theta(t) \end{bmatrix} \quad (8)$$

$$\boldsymbol{a}(t) = R\begin{bmatrix} -\dot{\theta}^2(t) - \dot{\varphi}^2(t)\sin^2\theta(t) \\ \ddot{\theta}(t) - \dot{\varphi}^2(t)\sin\theta(t)\cos\theta(t) \\ \ddot{\varphi}(t)\sin\theta(t) + 2\dot{\theta}(t)\dot{\varphi}(t)\cos\theta(t) \end{bmatrix} \quad (9)$$

The velocity module is:

$$|v(t)| = R\sqrt{\dot{\theta}^2(t) + \dot{\varphi}^2(t)\sin^2\theta(t)} \quad (10)$$

To set up the equations of motion for the system, we resort to the Lagrange equation, which states the following:

$$\frac{d}{dt}\left(\frac{\partial L(t)}{\partial \dot{q}_i}\right) - \frac{\partial L(t)}{\partial q_i} = Q_i(t) \quad (11)$$

where the Lagrangian is given by:

$$L(t) = T(t) - V(t) \quad (12)$$

with the kinetic energy and the potential energy are, respectively,

$$T(t) = \frac{1}{2}mv^2(t) = \frac{1}{2}mR^2\left(\dot{\theta}^2(t) + \dot{\varphi}^2(t)\sin^2\theta(t)\right) \quad (13)$$

$$V(t) = mgh(t) = V_0 - mgR\cos\theta(t) \quad (14)$$

Because it is seen that $V(t)/\partial\,\dot{q}_i = 0$, Eq. 11 becomes

$$\frac{d}{dt}\left(\frac{\partial T(t)}{\partial \dot{q}_i}\right) - \frac{\partial T(t)}{\partial q_i} + \frac{\partial V(t)}{\partial q_i} = Q_i(t) \quad (15)$$

As regards the first term of the left-hand side, we have:

$$\frac{\partial T(t)}{\partial \dot{R}} = 0 \quad (16)$$

$$\frac{\partial T(t)}{\partial \dot{\theta}} = mR^2\dot{\theta}(t) \quad (17)$$

$$\frac{\partial T(t)}{\partial \dot{\varphi}} = mR^2\dot{\varphi}(t)\sin^2\theta(t) \quad (18)$$

with the subsequent time derivatives being

$$\frac{d}{dt}\left(\frac{\partial T(t)}{\partial \dot{R}}\right) = 0 \quad (19)$$

$$\frac{d}{dt}\left(\frac{\partial T(t)}{\partial \dot{\theta}}\right) = mR^2\ddot{\theta}(t) \quad (20)$$

$$\frac{d}{dt}\left(\frac{\partial T(t)}{\partial \dot{\varphi}}\right) = mR^2\left(\ddot{\varphi}(t)\sin^2\theta(t) + \dot{\theta}(t)\dot{\varphi}(t)\sin 2\theta(t)\right) \quad (21)$$

For the second term of the left-hand side in Eq. 15, we have:

$$\frac{\partial T(t)}{\partial R} = mR\left(\dot{\theta}^2(t) + \dot{\varphi}^2(t)\sin^2\theta(t)\right) \quad (22)$$

$$\frac{\partial T(t)}{\partial \theta} = mR^2\dot{\varphi}^2(t)\sin\theta(t)\cos\theta(t) \quad (23)$$

$$\frac{\partial T(t)}{\partial \phi} = 0 \quad (24)$$

For the third term of the left-hand side in Eq. 15, we have:

$$\frac{\partial V(t)}{\partial R} = -mg\cos\theta(t) \quad (25)$$

$$\frac{\partial V(t)}{\partial \theta} = mgR\sin\theta(t) \quad (26)$$

$$\frac{\partial V(t)}{\partial \varphi} = 0 \quad (27)$$

Replacing the corresponding quantities in the Lagrange equation of motion [15], we obtain the three equations of motion:

$$-mR\left(\dot{\theta}^2(t) + \dot{\varphi}^2(t)\sin^2\theta(t)\right) - mg\cos\theta(t) = Q_R(t) \quad (28)$$

$$mR^2\left(\ddot{\theta}(t) - \dot{\varphi}^2(t)\sin\theta(t)\cos\theta(t)\right) + mgR\sin\theta(t) = Q_\theta(t) \quad (29)$$

$$mR^2\left(\ddot{\varphi}(t)\sin^2\theta(t) + 2\dot{\theta}(t)\dot{\varphi}(t)\sin\theta(t)\cos\theta(t)\right) = Q_\varphi(t) \quad (30)$$

These represent the dynamic equilibrium equations along r, θ, and φ, respectively. From the physical standpoint, the two latter actually represent the moment equilibrium equations about point O and about the z-axis, respectively, as seen in Figure 1.

The non-conservative forces acting on the mass m are the inertia forces $q_I(t) = -ma_{gS} = -m[a_{gR}(t)\ a_{g\theta}(t)\ a_{g\varphi}(t)]^T$ due to the accelerations in the Lagrangian coordinates and the reactive forces at the pad-sphere interface $q_F(t) = -\phi(t) = [\phi_R(t)\ \phi_\theta(t)\ \phi_\phi(t)]$, directed orthogonal to the surface, along the meridian tangent, and along the parallel tangent, respectively. In order to compute the generalized forces $Q(t)$ that fit into the equilibrium equations previously shown, the forces $q(t) = q_I(t) + q_F(t)$ must be multiplied by a so-called position matrix $R(t)$, as follows:

$$\mathbf{Q}(t) = \mathbf{R}(t)\mathbf{q}(t) \quad (31)$$

where $R(t)$ contains the distances from the moment poles (Figure 1):

$$\mathbf{R}(t) = \begin{bmatrix} 1 & 0 & 0 \\ 0 & R & 0 \\ 0 & 0 & R\sin\theta(t) \end{bmatrix} \quad (32)$$

The non-conservative generalized forces are therefore obtained as follows:

$$\boldsymbol{Q}(t) = \boldsymbol{Q}_I(t) + \boldsymbol{Q}_F(t) = \mathbf{R}(t)\{\boldsymbol{q}_I(t) + \boldsymbol{q}_F(t)\} = \mathbf{R}(t)\{-m\mathbf{a}_{gS}(t) + \boldsymbol{\phi}(t)\}$$
$$= \begin{bmatrix} 1 & 0 & 0 \\ 0 & R & 0 \\ 0 & 0 & R\sin\theta(t) \end{bmatrix} \left\{ -m \begin{bmatrix} a_{gR}(t) \\ a_{g\theta}(t) \\ a_{g\varphi}(t) \end{bmatrix} + \begin{bmatrix} \phi_R(t) \\ \phi_\theta(t) \\ \phi_\varphi(t) \end{bmatrix} \right\} \quad (33)$$

In regard to the inertia forces $Q_I(t)$, the relationship between the accelerations in the spherical coordinate system and those in the Cartesian coordinate system is (notice that $a_{gz}(t)$ has a negative sign because the z-axis is oriented downwards):

$$\boldsymbol{a}_{gS}(t) = \boldsymbol{S}_{C2S}(t)\boldsymbol{a}_{gC}(t)$$
$$= \begin{bmatrix} \sin\theta(t)\cos\varphi(t) & \sin\theta(t)\sin\varphi(t) & \cos\theta(t) \\ \cos\theta(t)\cos\varphi(t) & \cos\theta(t)\sin\varphi(t) & -\sin\theta(t) \\ -\sin\varphi(t) & \cos\varphi(t) & 0 \end{bmatrix} \begin{bmatrix} a_{gx}(t) \\ a_{gy}(t) \\ -a_{gz}(t) \end{bmatrix} \quad (34)$$

to obtain

$$\boldsymbol{a}_{gS}(t) = \begin{bmatrix} a_{gx}(t)\sin\theta(t)\cos\varphi(t) + a_{gy}(t)\sin\theta(t)\sin\varphi(t) - a_{gz}(t)\cos\theta(t) \\ a_{gx}(t)\cos\theta(t)\cos\varphi(t) + a_{gy}(t)\cos\theta(t)\sin\varphi(t) + a_{gz}(t)\sin\theta(t) \\ -a_{gx}(t)\sin\varphi(t) + a_{gy}(t)\cos\varphi(t) \end{bmatrix} \quad (35)$$

so that, finally, the inertia forces are:

$$\boldsymbol{Q}_I(t) = -m\mathbf{R}(t)\mathbf{a}_{gS}(t) = -m\mathbf{R}(t)\boldsymbol{S}_{C2S}(t)\boldsymbol{a}_{gC}(t)$$
$$= -m \begin{bmatrix} a_{gx}(t)\sin\theta(t)\cos\varphi(t) + a_{gy}(t)\sin\theta(t)\sin\varphi(t) - a_{gz}(t)\cos\theta(t) \\ R\big(a_{gx}(t)\cos\theta(t)\cos\varphi(t) + a_{gy}(t)\cos\theta(t)\sin\varphi(t) + a_{gz}(t)\sin\theta(t)\big) \\ R\big(-a_{gx}(t)\sin\varphi(t) + a_{gy}(t)\cos\varphi(t)\big)\sin\theta(t) \end{bmatrix} \quad (36)$$

As for the reactive forces $Q_F(t)$, it should be noted that $\varphi_R(t)$, that is the support reaction offered by the sphere normally to its surface, can be computed at any t from Eq. 28 as a function of the current $\theta(t)$ and $\phi(t)$ satisfying the two equations of motion 29 and 30, as follows:

$$\phi_R(t) = -\left(mR\left(\dot{\theta}^2(t) + \dot{\varphi}^2(t)\sin^2\theta(t)\right) + mg\cos\theta(t) + Q_R(t)\right)$$

$$= -m\begin{pmatrix} R\left(\dot{\theta}^2(t) + \dot{\varphi}^2(t)\sin^2\theta(t)\right) + g\cos\theta(t) + \\ +a_{gx}(t)\sin\theta(t)\cos\varphi(t) + a_{gy}(t)\sin\theta(t)\sin\varphi(t) - a_{gz}(t)\cos\theta(t) \end{pmatrix} \quad (37)$$

In case of frictional surface, the two reactions $\phi_\theta(t)$ and $\varphi_\phi(t)$ are obtained by multiplying the dynamic friction coefficient μ_d by the normal force applied by the moving pad on the sphere surface ($-\varphi_R(t)$), as follows:

$$\phi_\theta(t) = -\mu_d(-\phi_R(t))\cdot\mathrm{sgn}\left(\dot{\theta}(t)\right) = \mu_d\phi_R(t)\cdot\mathrm{sgn}\left(\dot{\theta}(t)\right) \quad (38)$$

$$\phi_\varphi(t) = -\mu_d(-\phi_R(t))\cdot\mathrm{sgn}(\dot{\varphi}(t)\sin\theta(t)) = \mu_d\phi_R(t)\cdot\mathrm{sgn}(\dot{\varphi}(t)\sin\theta(t)) \quad (39)$$

Notice that, in case of frictionless surface of the sphere, $\phi(t) = \phi_\varphi(t) = 0$. Also for the sake of simplicity, we disregard the distinction between static and dynamic friction coefficients.

Replacing the expressions of the non-conservative forces due to friction into the equations of motions 29 and 30, we obtain the following:

$$mR^2\left(\ddot{\theta}(t) - \dot{\varphi}^2(t)\sin\theta(t)\cos\theta(t)\right) + mgR\sin\theta(t)$$
$$= Q_{I\theta}(t) + R\mu_d\phi_R(t)\cdot\mathrm{sgn}\left(\dot{\theta}(t)\right) \quad (40)$$

$$mR^2\left(\ddot{\varphi}(t)\sin^2\theta(t) + 2\dot{\theta}(t)\dot{\varphi}(t)\sin\theta(t)\cos\theta(t)\right)$$
$$= Q_{I\varphi}(t) + R\mu_d\phi_R(t)\sin\theta(t)\cdot\mathrm{sgn}(\dot{\varphi}(t)\sin\theta(t)) \quad (41)$$

By replacing the expressions for the normal force $\phi_R(t)$ found in Eq. 37 and for the inertia forces due to seismic action found in Eq. 36, we finally obtain the equations of motion of a particle P having mass m, moving on a frictional sphere surface with radius R, along meridians $\theta(t)$ and parallels $\varphi(t)$, under 3D ground motion excitation:

$$mR^2\left(\ddot{\theta}(t) - \dot{\varphi}^2(t)\sin\theta(t)\cos\theta(t)\right) + mgR\sin\theta(t)$$
$$= -mR\left(a_{gx}(t)\cos\theta(t)\cos\varphi(t) + a_{gy}(t)\cos\theta(t)\sin\varphi(t) + a_{gz}(t)\sin\theta(t)\right)$$
$$+ -mR\mu_d\begin{pmatrix} R\left(\dot{\theta}^2(t) + \dot{\phi}^2(t)\sin^2\theta(t)\right) + g\cos\theta(t) + \\ +a_{gx}(t)\sin\theta(t)\cos\varphi(t) + a_{gy}(t)\sin\theta(t)\sin\varphi(t) \\ -a_{gz}(t)\cos\theta(t) \end{pmatrix}\cdot\mathrm{sgn}\left(\dot{\theta}(t)\right) \quad (42)$$

$$
\begin{aligned}
&mR^2\left(\ddot{\varphi}(t)\sin\theta(t)+2\dot{\theta}(t)\dot{\varphi}(t)\cos\theta(t)\right)= \\
&-mR\left(-a_{gx}(t)\sin\varphi(t)+a_{gy}(t)\cos\varphi(t)\right)+ \\
&-mR\mu_d\left[\begin{array}{l} R\left(\dot{\theta}^2(t)+\dot{\varphi}^2(t)\sin^2\theta(t)\right)+g\cos\theta(t)+ \\ \left(\begin{array}{l} a_{gx}(t)\sin\theta(t)\cos\varphi(t)+a_{gy}(t)\sin\theta(t)\sin\varphi(t)+ \\ -a_{gz}(t)\cos\theta(t) \end{array}\right) \end{array}\right]\cdot\mathrm{sgn}(\dot{\varphi}(t)\sin\theta(t))
\end{aligned}
\tag{43}
$$

The aforementioned equations can be further simplified into the following:

$$
\begin{aligned}
&R\left(\ddot{\theta}(t)-\dot{\varphi}^2(t)\sin\theta(t)\cos\theta(t)\right)+g\sin\theta(t) \\
&\quad=-\left(a_{gx}(t)\cos\theta(t)\cos\varphi(t)+a_{gy}(t)\cos\theta(t)\sin\varphi(t)+a_{gz}(t)\sin\theta(t)\right) \\
&\quad\quad+-\mu_d\left(\begin{array}{l} R\left(\dot{\theta}^2(t)+\dot{\varphi}^2(t)\sin^2\theta(t)\right)+g\cos\theta(t)+ \\ +a_{gx}(t)\sin\theta(t)\cos\varphi(t)+a_{gy}(t)\sin\theta(t)\sin\varphi(t) \\ -a_{gz}(t)\cos\theta(t) \end{array}\right)\cdot\mathrm{sgn}\left(\dot{\theta}(t)\right)
\end{aligned}
\tag{44}
$$

$$
\begin{aligned}
&R\left(\ddot{\varphi}(t)\sin\theta(t)+2\dot{\theta}(t)\dot{\varphi}(t)\cos\theta(t)\right) \\
&\quad=-\left(-a_{gx}(t)\sin\varphi(t)+a_{gy}(t)\cos\varphi(t)\right) \\
&\quad\quad+-\mu_d\left[\begin{array}{l} R\left(\dot{\theta}^2(t)+\dot{\varphi}^2(t)\sin^2\theta(t)\right)+g\cos\theta(t)+ \\ \left(\begin{array}{l} a_{gx}(t)\sin\theta(t)\cos\varphi(t)+a_{gy}(t)\sin\theta(t)\sin\varphi(t)+ \\ -a_{gz}(t)\cos\theta(t) \end{array}\right) \end{array}\right]\cdot\mathrm{sgn}(\dot{\varphi}(t)\sin\theta(t))
\end{aligned}
\tag{45}
$$

where it can be seen that the mass m cancels out.

3 Dynamic Stiffness of a Friction Pendulum

Having defined the full 2D equations of motions, it comes all too natural to compute the exact stiffness of the FP in dynamic conditions, with complete consideration of the interaction between the two DOFs, the polar angle $\theta(t)$ and the azimuth angle $\phi(t)$. The equations will be initially developed in large oscillations and then simplified to the case of small oscillations.

3.1 Large oscillations

The equation of motion relevant to the degree of freedom $\theta(t)$ obtained in Eq. 44 can be divided by R and rearranged in order of derivative as follows:

$$\ddot{\theta}(t)+\dot{\theta}^2(t)$$
$$+\left[\begin{array}{l}\dfrac{g}{R}-\dot{\varphi}^2(t)\cos\theta(t)+\dfrac{a_{gz}(t)}{R}+\\ +\mu_d\left(\begin{array}{l}\dfrac{a_{gx}(t)}{R}\cos\varphi(t)+\dfrac{a_{gy}(t)}{R}\sin\varphi(t)+\\ +\dot{\varphi}^2(t)\sin\theta(t)\end{array}\right)\cdot\mathrm{sgn}\left(\dot{\theta}(t)\right)\end{array}\right]\sin\theta(t)$$
$$+\frac{a_{gx}(t)}{R}\cos\theta(t)\cos\varphi(t)+\frac{a_{gy}(t)}{R}\cos\theta(t)\sin\varphi(t)$$
$$+\mu_d\left[\frac{g}{R}\cos\theta(t)-\frac{a_{gz}(t)}{R}\cos\theta(t)\right]\mathrm{sgn}\left(\dot{\theta}(t)\right)=0 \quad (46)$$

The third term represents the recentering force of the FP. When divided by the (large) displacement $\sin\theta(t)$, it yields the 2D dynamic stiffness along the meridian during forced oscillations:

$$k_\theta(t)=\frac{g}{R}-\dot{\varphi}^2(t)\cos\theta(t)+\frac{a_{gz}(t)}{R}$$
$$+\mu_d\left(\begin{array}{l}\dfrac{a_{gx}(t)}{R}\cos\varphi(t)+\dfrac{a_{gy}(t)}{R}\sin\varphi(t)+\\ +\dot{\varphi}^2(t)\sin\theta(t)\end{array}\right)\cdot\mathrm{sgn}\left(\dot{\theta}(t)\right) \quad (47)$$

This equation is the most general expression of the FP stiffness, and as a matter of fact, it contains, in the first term g/R, the stiffness usually attributed to FP devices considered in their 1D behavior. All other terms in the right-hand side of the equation contribute to the stiffness by taking into account, respectively, the friction component, the vertical component of the input acceleration, and above all, the azimuth angular velocity of the pad along the parallels of the sphere. This term, as it will be shown later, is the one that mostly contributes to modifying the stiffness during the dynamic motion.

It is also interesting to notice that, as opposed to the case of the 1D pendulum equations yielding a constant stiffness, that obtained with the 2D equations is a function of time and as such it changes during the motion. This implies, for example, that in FP-isolated buildings, the continuous coincidence between center of mass and center of stiffness might not be guaranteed.

Finally, it is worth noticing that, for the cases of free vibrations and absence of friction, Eq. 47 becomes, respectively,

$$k_\theta(t)=\frac{g}{R}-\dot{\varphi}^2(t)\left[\cos\theta(t)-\mu_d\sin\theta(t)\cdot\mathrm{sgn}\left(\dot{\theta}(t)\right)\right] \quad (48)$$

$$k_\theta(t)=\frac{g}{R}-\dot{\varphi}^2(t)\cos\theta(t)+\frac{a_{gz}(t)}{R} \quad (49)$$

If we set $a_{gZ}(t) = 0$ in the latter equation, we find that the FP stiffness can actually become 0 when, at any time t, the following condition is satisfied:

$$\dot{\varphi}(t) = \sqrt{\frac{g}{R\cos\theta(t)}} \quad (50)$$

This is the angular velocity that would keep the pad on a stable orbit about the azimuth z-axis, thus transforming the FP into a conical pendulum. The velocity depends on the polar angle $\theta(t)$. The wider the conical pendulum is, the higher the velocity to keep its orbit stable has to be.

Finally, it should be observed that if the angular velocity is such that

$$\dot{\varphi}(t) > \sqrt{\frac{g + a_{gz}(t)}{R\cos\theta(t)}} \quad (51)$$

then the FP stiffness can even become negative. Both of the previously described situations may actually occur during a 2D FP motion, even if for a short time.

3.2 Small oscillations

Under the hypothesis of small oscillations about the 'bottom' of the sphere, the following assumptions hold:

$$\sin\theta \approx \theta\ ,\ \sin^2\theta \approx 0,\ \text{ and } \cos\theta \approx 1$$

Therefore, the dynamic stiffness given in Eq. 47 simplifies to:

$$k_\theta(t) = \frac{g}{R} - \dot{\varphi}^2(t) + \frac{a_{gz}(t)}{R} + \mu_d\left(\frac{a_{gx}(t)}{R}\cos\varphi(t) + \frac{a_{gy}(t)}{R}\sin\varphi(t) + \dot{\varphi}^2(t)\theta(t)\right)\mathrm{sgn}\left(\dot{\theta}(t)\right) \quad (52)$$

This, multiplied by $\theta(t)$, gives the recentering force of the FP.

Again, in case of free vibrations and absence of friction, the stiffness becomes, respectively,

$$k_\theta(t) = \frac{g}{R} - \dot{\varphi}^2(t)\left[1 - \mu_d\theta(t)\cdot\mathrm{sgn}\left(\dot{\theta}(t)\right)\right] \quad (53)$$

$$k_\theta(t) = \frac{g}{R} - \dot{\varphi}^2(t) + \frac{a_{gz}(t)}{R} \quad (54)$$

3.3 Pad moving on a circle (one-dimensional pendulum)

The equation of motion of the 1D pendulum can be found as a particular case of Eq. 44, where $\varphi_t = const.$, for example 0°, along the x-axis:

$$R\ddot{\theta}(t) + g\sin\theta(t) =$$
$$-\left(a_{gx}(t)\cos\theta(t) + a_{gz}(t)\sin\theta(t)\right) +$$
$$-\mu_d\left[R\dot{\theta}^2(t) + g\cos\theta(t) + a_{gx}(t)\sin\theta(t) - a_{gz}(t)\cos\theta(t)\right]\cdot\mathrm{sgn}\left(\dot{\theta}(t)\right) \quad (55)$$

which, under the hypothesis of small oscillations, becomes

$$R\ddot{\theta}(t) + g\theta(t)$$
$$= -\left(a_{gx}(t) + a_{gz}(t)\theta(t)\right)$$
$$+ - \mu_d\left[R\dot{\theta}^2(t) + g + \left(a_{gx}(t)\theta(t) - a_{gz}(t)\right)\right]\cdot\mathrm{sgn}\left(\dot{\theta}(t)\right) \quad (56)$$

Therefore, for the case of small oscillation with friction, the stiffness is as follows:

$$k_\theta(t) = \frac{g}{R} + \frac{a_{gz}(t)}{R} + \mu_d\frac{a_{gx}(t)}{R}\cdot\mathrm{sgn}\left(\dot{\theta}(t)\right) \quad (57)$$

This is a more general equation than that usually assumed for 1D pendulums, that is $k_\theta = g/R$, as it contains the contributions of the friction component and the vertical acceleration. However, because the friction coefficient is in general very low, that contribution can be neglected with respect to that of the first term, while the second term, if there is a vertical acceleration, cannot.

When considering the cases of free vibrations and absence of friction, Eq. 57 becomes, respectively,

$$k_\theta(t) = \frac{g}{R} \quad (58)$$

$$k_\theta(t) = \frac{g}{R} + \frac{a_{gz}(t)}{R} \quad (59)$$

Thus, the stiffness in Eq. 58, usually assumed for FP bearings, actually represents that of a 1D pendulum, under the hypothesis of small oscillations and free vibrations in absence of friction, which is certainly inappropriate to represent real cases.

3.4 Pad moving on two intersecting circles (‘1.5D’ pendulum)

Previously, for the sake of conciseness, we have defined as ‘1.5D’ pendulum the one obtained by considering the motion of two 1D pendulums oscillating in two orthogonal planes intersecting at the *z*-axis. The two responses, which are however independent, are then vectorially combined at any *t*, to obtain the overall motion. This gives rise to a set of two equations, which can be obtained as particular cases of Eq. 44, where $\varphi_t = const.$, for example 0°, along the *x*-axis, and 90 ° along the *y*-axis:

$$R\ddot{\theta}_x(t) + g\sin\theta_x(t) =$$
$$-\left(a_{gx}(t)\cos\theta_x(t) + a_{gz}(t)\sin\theta_x(t)\right) +$$
$$-\mu_d\left[R\dot{\theta}_x^2(t) + g\cos\theta_x(t) + a_{gx}(t)\sin\theta_x(t) - a_{gz}(t)\cos\theta_x(t)\right]\cdot\mathrm{sgn}\left(\dot{\theta}_x(t)\right) \quad (60)$$

$$R\ddot{\theta}_y(t) + g\sin\theta_y(t) =$$
$$-\left(a_{gy}(t)\cos\theta_y(t) + a_{gz}(t)\sin\theta_y(t)\right) +$$
$$-\mu_d\left[R\dot{\theta}_y^2(t) + g\cos\theta_y(t) + a_{gy}(t)\sin\theta_y(t) - a_{gz}(t)\cos\theta_y(t)\right]\cdot\mathrm{sgn}\left(\dot{\theta}_y(t)\right) \quad (61)$$

which, under the hypothesis of small oscillations, become:

$$R\ddot{\theta}_x(t) + g\theta_x(t) =$$
$$-\left(a_{gx}(t) + a_{gz}(t)\theta_x(t)\right) +$$
$$-\mu_d\left[R\dot{\theta}_x^2(t) + g + \left(a_{gx}(t)\theta_x(t) - a_{gz}(t)\right)\right]\cdot\mathrm{sgn}\left(\dot{\theta}_x(t)\right) \quad (62)$$

$$R\ddot{\theta}_y(t) + g\theta_y(t) =$$
$$-\left(a_{gy}(t) + a_{gz}(t)\theta_y(t)\right) +$$
$$-\mu_d\left[R\dot{\theta}_y^2(t) + g + \left(a_{gy}(t)\theta_y(t) - a_{gz}(t)\right)\right]\cdot\mathrm{sgn}\left(\dot{\theta}_y(t)\right) \quad (63)$$

As seen, the two equations are uncoupled and are therefore integrated independently of each other. The respective motion amplitude is then obtained as

$$\theta(t) = \sqrt{\theta_x^2(t) + \theta_y^2(t)} \quad (64)$$

and the azimuth angle as

$$\varphi(t) = \tan^{-1}\frac{\theta_y(t)}{\theta_x(t)} \quad (65)$$

Therefore, for the case of small oscillations with friction, the stiffness is as follows:

$$k_\theta(t) = \frac{F_\theta(t)}{\theta(t)} = \frac{\sqrt{F_x^2(t) + F_y^2(t)}}{\sqrt{\theta_x^2(t) + \theta_y^2(t)}}$$
$$= \sqrt{\frac{\left\{\begin{array}{l}\left[\dfrac{g}{R} + \dfrac{a_{gz}(t)}{R} + \dfrac{\mu_d}{R}a_{gx}(t)\cdot\mathrm{sgn}\left(\dot{\theta}_x(t)\right)\right]^2\theta_x^2(t) + \\ + \left[\dfrac{g}{R} + \dfrac{a_{gz}(t)}{R} + \dfrac{\mu_d}{R}a_{gy}(t)\cdot\mathrm{sgn}\left(\dot{\theta}_y(t)\right)\right]^2\theta_y^2(t)\end{array}\right\}}{\theta_x^2(t) + \theta_y^2(t)}} \quad (66)$$

This quite cumbersome expression considerably simplifies when considering the cases of free vibrations and the absence of friction, so that Eq. 66 becomes, respectively,

$$k_\theta(t) = \frac{g}{R} \quad (67)$$

$$k_\theta(t) = \frac{g}{R} + \frac{a_{gz}(t)}{R} \quad (68)$$

which have the appealing property of being the same as the 1D pendulum's seen in Eqs. 58 and 59.

4 Adding a Third DOF: Temperature

This section is devoted to present how temperature can be simply included in the proposed 2D model as a third DOF, in addition to ϕ and θ. When the pad covered with a low friction material moves along the stainless steel concave surface, the friction between the two generates heat that, in turn, affects the friction coefficient and consequently the overall effectiveness of the isolation system. During the motion the contact surface remains the same for the pad, while it changes continuously for the concave surface. For this reason, and also because the mass of the pad is much smaller than that of the concave surface, the temperature increase is much higher in the former than in the latter. These considerations are all documented in a detailed manner in several past works, for example, [19, 20], and especially in [17], where a heating theory, including the effects of the size of the moving slider in comparison with the amplitude of motion, was developed for general 2D motion and then validated by 1D experiments.

If a pure 1D model was used, the contact surface would lie along a circle, and heat transfer would occur along the same curved line. In general motions, as the 1.5D considered in [17] and the 2D derived in the model here proposed, the contact surface lies along the generic trajectory taken by the pad on the sphere, and heat transfer occurs at points that continuously change. Therefore, it is acknowledged that if the trajectories described by the 1.5D and 2D FP do not significantly differ, the modeling of temperature variation will not differ as well.

As for the 2D model here derived, in terms of formulation the temperature is included in the set of differential equations. Then, the friction coefficient can be easily made dependent on the temperature, according to the studies and formulations already available in literature and widely experimentally proved.

However, because this goes beyond the scope of this paper that wants to propose a complete 2D mechanical model that includes the temperature, thereafter, we will assume that the temperature in the concave surface is constant in the average and equal to the environmental temperature, while

temperature in the pad varies. Also, in these first developments, we will assume that the friction coefficient is independent of the temperature.

The first principle of thermodynamics for a closed system, made from the pad only, can be written as follows:

$$\dot{E}_{pad} = \dot{E}_{in} - \dot{E}_{out} + \dot{E}_g - \dot{L} \quad (69)$$

where $\dot{E}_{pad}$ is the thermal power stored in the pad, $\dot{E}_{in}$ is the thermal power input (0 J/s in this case), $\dot{E}_{out}$ is the thermal power output (from the pad to the concave element, due to conduction), $\dot{E}_g$ is the thermal power internally generated by the system through friction, and $\dot{L}$ is the mechanical power (0 J/s in this case). All quantities are expressed as energy per time unit.

The first term vanishes if the system is stationary. If it is not stationary, the energy stored in the pad per time unit is as follows:

$$\dot{E}_{Sist} = m_{pad} c \dot{T}_{pad} \quad (70)$$

where m_{pad} is the mass of the pad and c is the specific heat of stainless steel, equal to 420 J/kg °C.

We assume that the thermal power output occurs only because of conduction between the two parts (the pad and the surface) and that no convection exchange occurs with the external environment. The heat flow rate (measured in $W = J/s$) at the pad–surface interface A_{pad} is as follows:

$$\dot{Q} = \dot{E}_{out} = h_c \left(T_{pad} - T_{sur}\right) A_{pad} \quad (71)$$

where h_c is the heat transfer coefficient, which for stainless steel is 16 J/s m^2 °C.

Finally, the thermal power internally generated by the system through friction is given as the product of the friction force times the velocity, that is,

$$\dot{E}_g = \phi_\theta R \dot{\theta} + \phi_\varphi R \dot{\varphi} \sin\theta \quad (72)$$

which can be rewritten as follows:

$$\dot{E}_g = \mu_d \phi_R R \left(\dot{\theta} \cdot \operatorname{sgn}\left(\dot{\theta}\right) + \dot{\varphi} \sin\theta \cdot \operatorname{sgn}\left(\dot{\varphi} \sin\theta\right)\right) = \dot{E}_g = \mu_d \phi_R R \left(\left|\dot{\theta}\right| + \left|\dot{\varphi} \sin\theta\right|\right) \quad (73)$$

Then, the energy rate balance is finally written for the pad:

$$m_{pad} c \dot{T}_{pad} = \mu_d \phi_R R \left(\left|\dot{\theta}\right| + \left|\dot{\varphi} \sin\theta\right|\right) - h_c \left(T_{pad} - T_{sur}\right) A_{pad} \quad (74)$$

Notice that, for the purpose of this work, the friction coefficient has been assumed as independent of temperature. This allows uncoupling these equations from the dynamic ones. Further studies are under way to deal with the coupled thermo-mechanical equations of motion.

By replacing the expression for $\phi_r(t)$, Eq. 74 becomes the following:

$$m_{pad}c\dot{T}_{pad} = m\mu_d R\left[\begin{array}{l} R\left(\dot{\theta}^2 + \dot{\varphi}^2\sin^2\theta\right) + g\cos\theta + \\ +\left(a_{gx}\sin\theta\cos\varphi + a_{gy}\sin\theta\sin\varphi - a_{gz}\cos\theta\right) \end{array}\right]$$
$$\left(\left|\dot{\theta}\right| + \left|\dot{\varphi}\sin\theta\right|\right) - h_c\left(T_{pad} - T_{sur}\right)A_{pad} \quad (75)$$

where the mass m pertains to the load carried by the device.

The preceding equation can be divided by $m_{pad}c$, to obtain:

$$\dot{T}_{pad} = \frac{m}{m_{pad}c}\mu_d R\left[\begin{array}{l} R\left(\dot{\theta}^2 + \dot{\varphi}^2\sin^2\theta\right) + g\cos\theta + \\ +\left(a_{gx}\sin\theta\cos\varphi + a_{gy}\sin\theta\sin\varphi - a_{gz}\cos\theta\right) \end{array}\right]$$
$$\left(\left|\dot{\theta}\right| + \left|\dot{\varphi}\sin\theta\right|\right) - h_c\left(T_{pad} - T_{sur}\right)A_{pad} \quad (76)$$

The 'thermal diffusivity' $\alpha = h_c/\rho c$ is introduced, where ρ is the mass density of stainless steel, to obtain the equation relevant to the 'third' DOF of the FP:

$$\dot{T}_{pad} = m\frac{\mu_d}{m_{pad}c}R\left[\begin{array}{l} R\left(\dot{\theta}^2 + \dot{\varphi}^2\sin^2\theta\right) + g\cos\theta + \\ +\left(a_{gx}\sin\theta\cos\varphi + a_{gy}\sin\theta\sin\varphi - a_{gz}\cos\theta\right) \end{array}\right]$$
$$\left(\left|\dot{\theta}\right| + \left|\dot{\varphi}\sin\theta\right|\right) - \frac{\alpha}{h_{pad}}\left(T_{pad} - T_{sur}\right) \quad (77)$$

5 Parametric Study

For assessing the effect of some basic parameters on the overall response of the 2D FP, an extended parametric study was conducted. The parameters considered are the following:

the type of earthquake excitation – bi-directional or tri-directional – accounted through $a_{gz} = 0$ or $a_{gz} \neq 0$ to simulate far-field or near-field earthquakes;

the PSD frequency content associated to three soil types: firm (F), medium (M), soft (S);

the sphere radius, $R = 3$, 4, and 5 m; and

the friction coefficient, $\mu_d = 0.006$, 0.02, and 0.06.

The results of some selected cases are presented either as time histories – when it is important to focus on certain features of the FP response – or as trajectories and maximum displacements in the horizontal plan – when a comparison between 1.5D and 2D FPs is needed.

Then, the results of the whole parametric study – deriving from the combination of all parameters listed previously – are presented as the average of the maximum displacement obtained over 20 analyses, under the acceleration time histories generated from the corresponding PSD function. The intensity of the PGA was kept constant and equal to 0.35 g, while the

parameters of the PSD function pertaining to firm, medium, and soft soil types are those given by Der Kiureghian and Neuenhofer [23].

The first case study presented in detail is that of a tri-directional earthquake excitation in soil type F, whose components in the x, y, and z directions are shown in Figure 2. Under this input acceleration, the response of four 2D FPs is analyzed, that is, (a) $R = 5$ m and $\mu_d = 0.006$, (b) $R = 5$ m and $\mu_d = 0.06$, (c) $R = 3$ and $\mu_d = 0.006$, and (d) $R = 3$ m and $\mu_d = 0.02$.

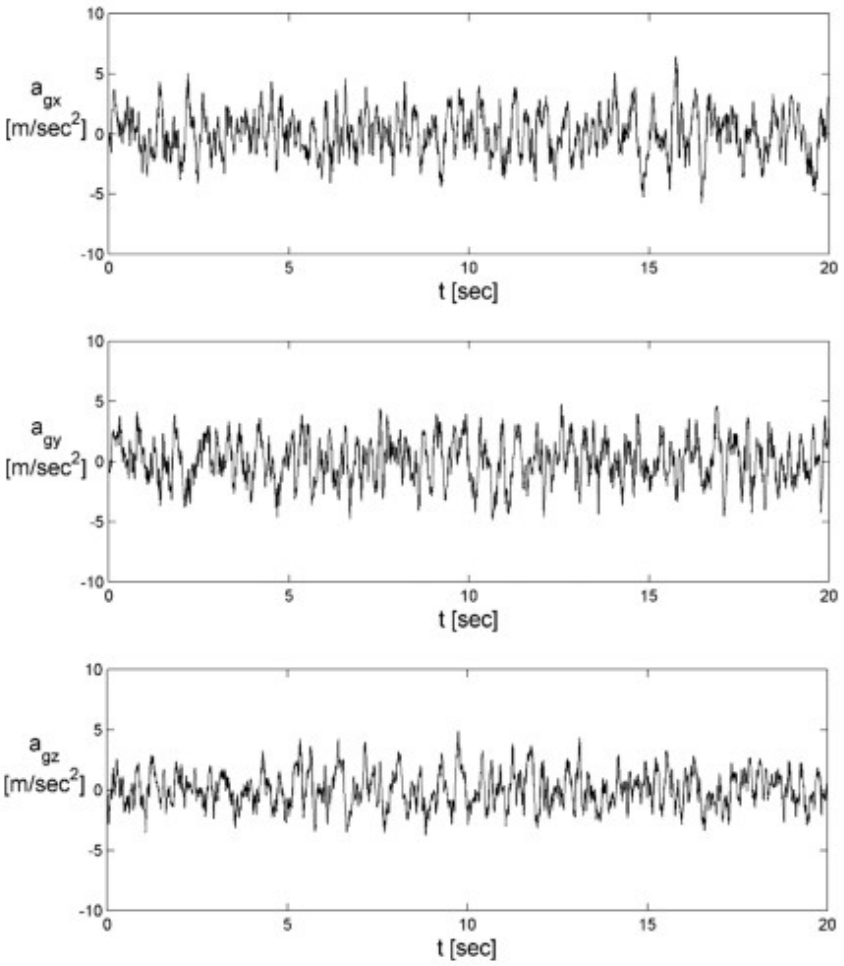

Figure 2. Stationary part of accelerograms in (a) x, (b) y, and (c) z directions for soil type F.

Figure 3 (a–d) reports the trajectory of the 2D FPs in the xyz space derived from Eq. 44 and 45 under the hypothesis of large oscillations.

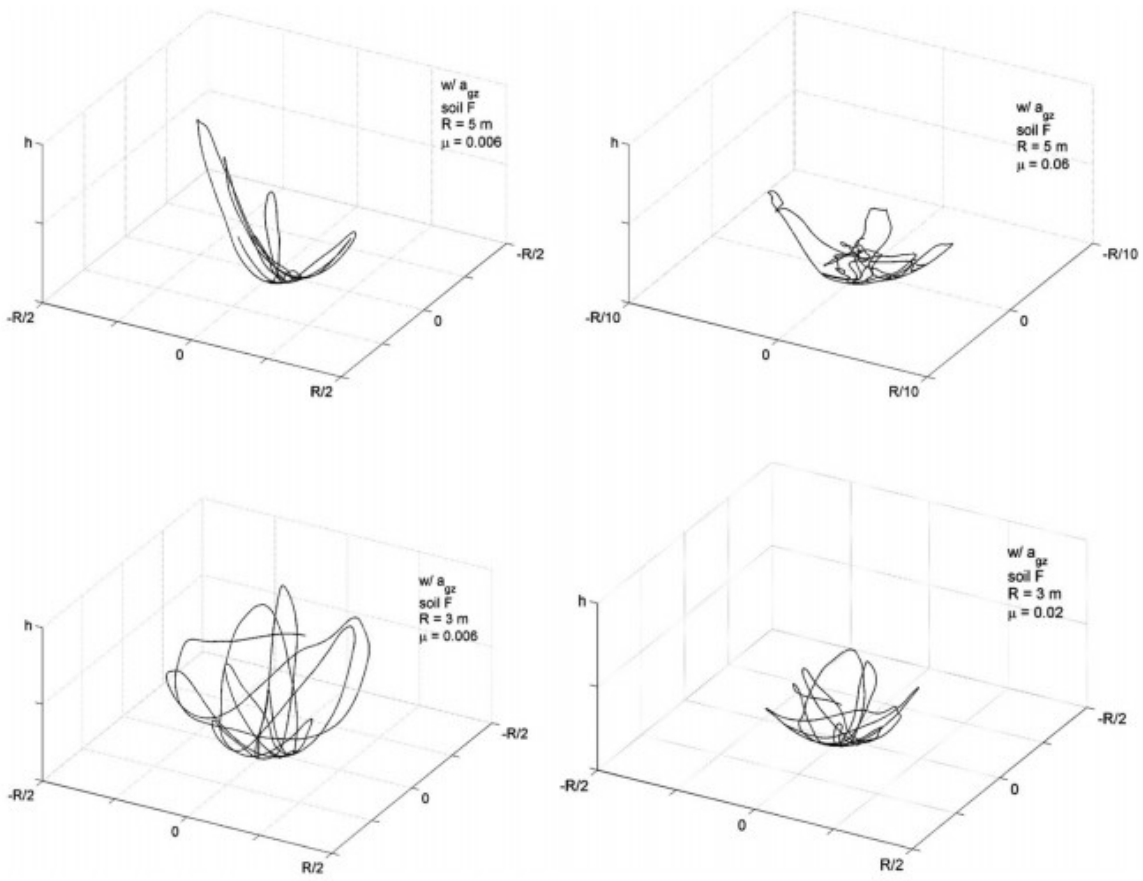

Figure 3. Trajectory of the pad on the sphere in the *xyz* space: cases a–d.

Then the trajectory of the same 2D FPs – a–d – is compared with that of the corresponding 1.5D FPs in the *xy* plan (Figure 4), still under the hypothesis of large oscillations, according to Eqs. 60-61, 64, and 65.

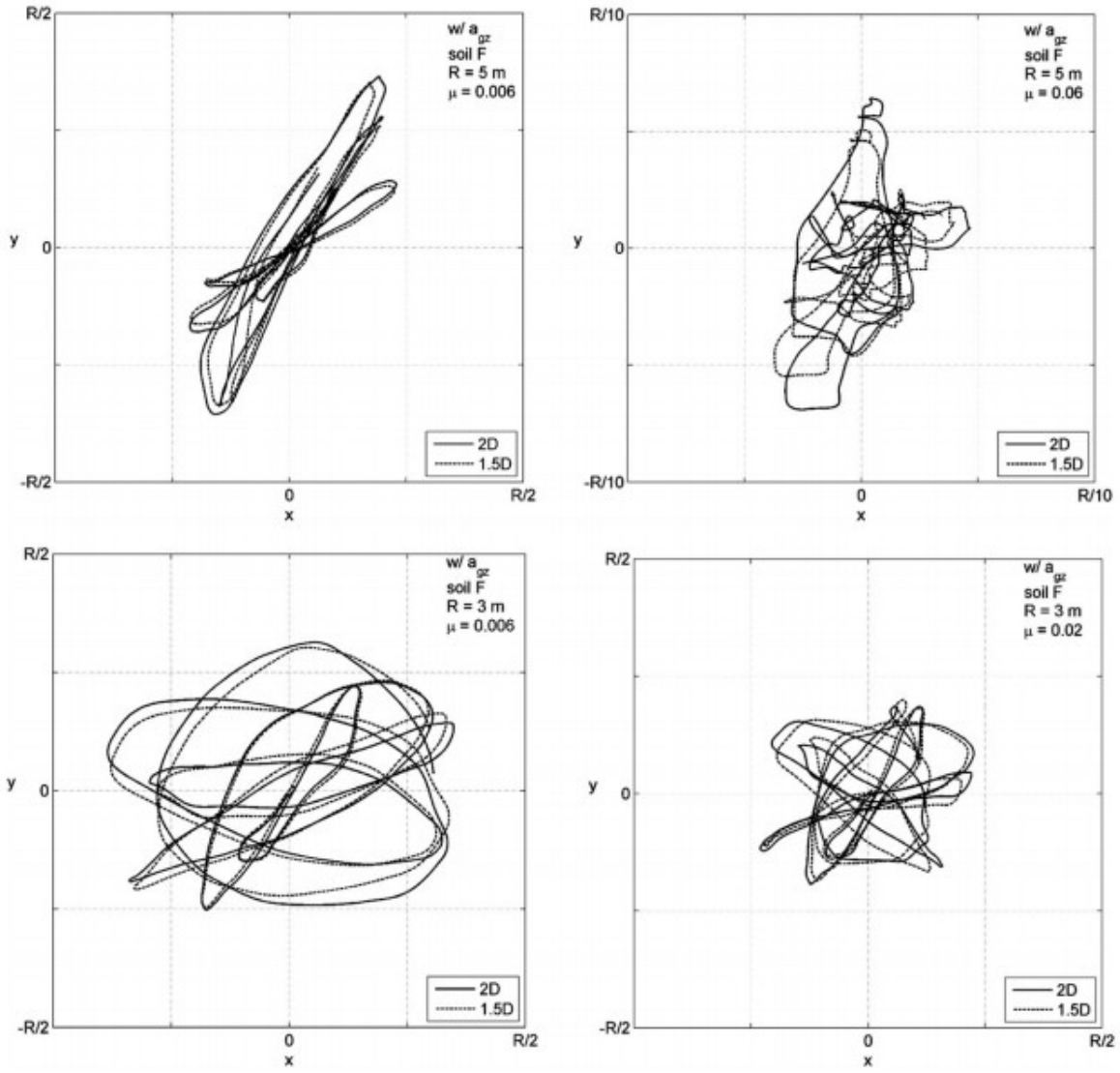

Figure 4. Trajectories of the pad on the *xy* plan: comparison 1.5D versus 2D for cases a–d.

First, as expected, with the same earthquake and FP's geometry, see solid lines for cases a–b and c–d, respectively, the maximum displacement is substantially affected by the friction coefficient: it reduces about five times when increasing the friction coefficient from 0.006 to 0.06 for $R = 5$ m and about two times when increasing the friction coefficient from 0.006 to 0.02 for $R = 3$ m. Also, looking at the magnitude of the maximum displacement, it may be worth noticing that the pad moves over $R/4$, usually assumed as design limit for single FPs (cases a and c). These should be regarded as pure theoretical cases, reported just for the purpose of the parametric study.

Then, from the comparison between the trajectories of the 1.5D and 2D FPs, the difference in the response of the two models is shown to be significant: in fact, in all four cases shown in Figure 4, the 1.5D FPs underestimate the

maximum displacement of the pad, with a difference that varies from about 5% for case c ($R = 3$ m, $\mu_d = 0.006$) up to 20% for case b ($R = 5$ m, $\mu_d = 0.06$).

Figure 5 shows κ time histories of the four 2D FPs, where $\kappa = k_{\theta,2D}/k_{\theta,1D}$ is the ratio of the actual stiffness of the 2D FPs, Eq. 47, to the stiffness of the corresponding 1D FPs as currently evaluated, Eq. 67.

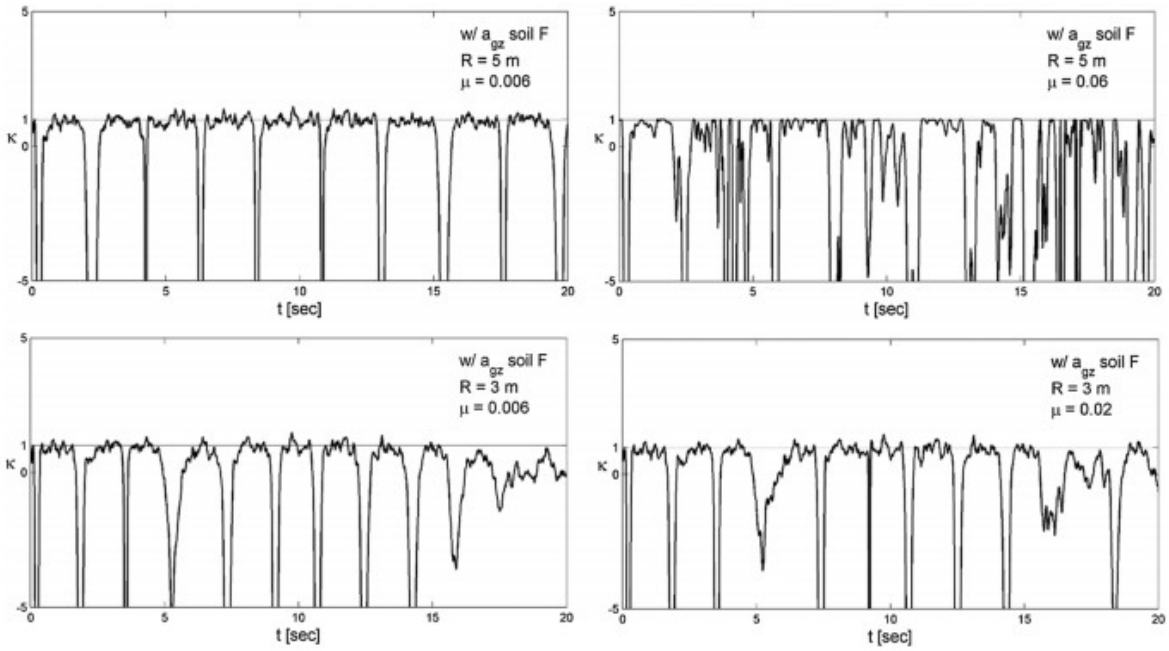

Figure 5. κ time history: cases a–d.

As already pointed out, the proposed formulation allows the stiffness of the FP to be expressed as function of time so to evaluate how it changes in response to the input acceleration and accounting for the actual position and velocity of the pad on the sphere.

The curves in the plots of Figure 5 show the FPs' stiffness variation and allow deriving the force acting on the pad once its position θ is known.

Overall, these curves show how κ fluctuates around 1, with a remarkable variation in the range <1, as especially evident in case b.

The second case study is that of a bi-directional earthquake excitation, simulating a far-field earthquake, in soil type S, whose components in the x and y directions are shown in Figure 6. The response of four 2D FPs is presented, and then a comparison with the performance of the corresponding 1.5D FPs is discussed. The FPs considered for these analyses are as follows: (e) $R = 4$ m and $\mu_d = 0.006$, (f) $R = 4$ m and $\mu_d = 0.02$, (g) $R = 5$ m and $\mu_d = 0.02$, and (h) $R = 5$ m and $\mu_d = 0.06$.

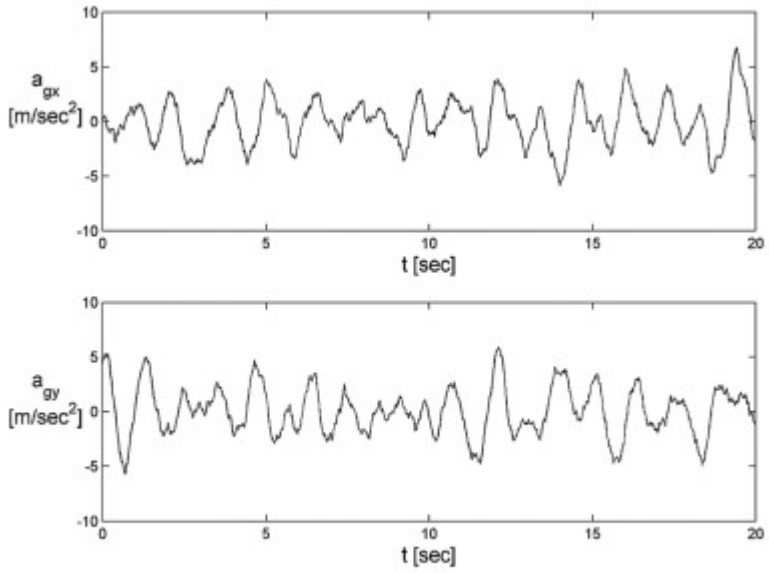

Figure 6. Accelerograms in (a) *x* and (b) *y* directions for soil type S.

Figure 7 shows the comparison between the 2D and 1.5D FPs in the *xy* plan. For the cases under consideration, there is still a variation in the maximum displacement when increasing the friction coefficient for the same FP and in response to the same earthquake, even if not so noticeable as for the case of soil F: the difference is around 18% and 25% when comparing plots a–b and c–d of Figure 7, respectively.

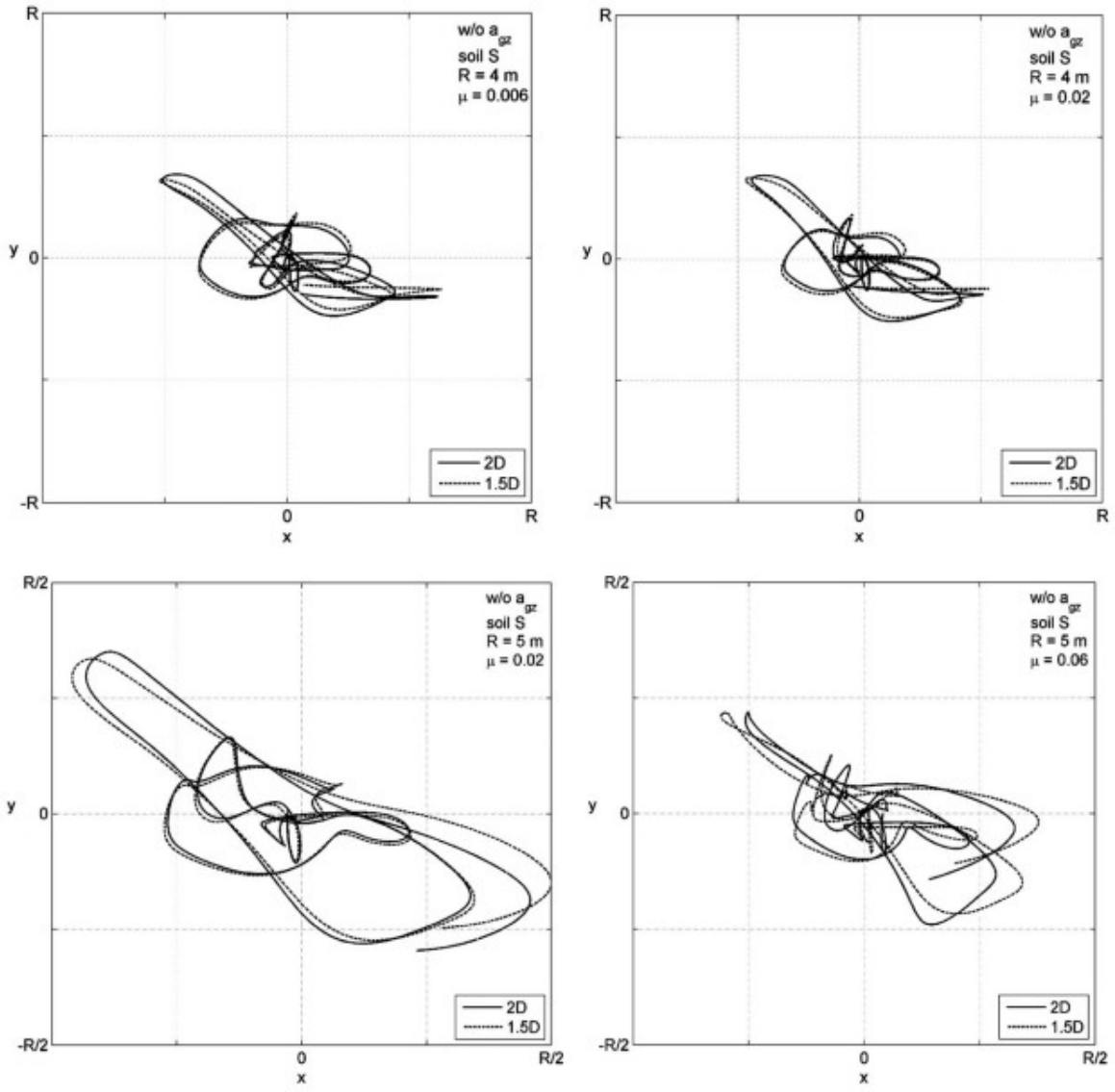

Figure 7. Trajectories of the pad on the *xy* plan: comparison 1.5D versus 2D for cases e–h.

As for the estimate of the maximum displacement derived with the 1.5D and 2D formulations, still under the large oscillations hypothesis, in all analyzed cases, the 1.5D FP considerably overestimates the maximum displacement of the pad, with a difference that varies from about 6% for cases e–g up to 15% for case h.

Figure 8 shows κ time history for e–h 2D FPs, calculated with the same method adopted for the previous case study: the curves, which lay in the $\kappa < 1$ area of the plots, show how the stiffness changes at each time step and clearly prove that, for the analyzed cases, the 1D FP formulation currently adopted fails in assuming a constant stiffness for the FP throughout the motion.

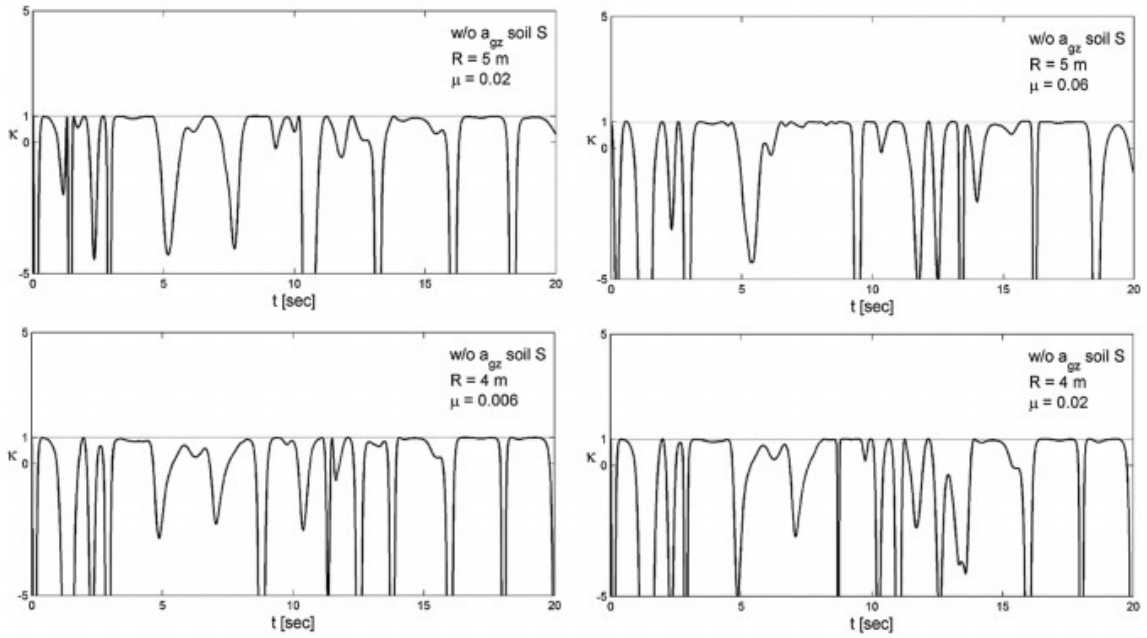

Figure 8. κ time history: cases e–h.

It may be worth underlining that the two case studies here presented aim at showing the response of different typologies of FPs to two random earthquakes. To have a statistical estimate of the results derived with the 1.5D and 2D models, a wider parametric study was developed over 20 near-field and far-field earthquakes, for three different types of soil and three different values of FP's radius and friction coefficient. These results are shown at the end of this section.

The results of the whole parametric study are summarized in Figure 9. The comparison between the 1.5D and 2D FPs is made in terms of maximum displacements of the pad on the surface during the 20-s stationary motion. The values reported in both plots represent the mean, over 20 earthquakes, of the ratio of the maximum displacement of the 1.5D FP to that of the 2D FP. The mean of the ratio has been computed as a second-order approximation under the hypothesis (verified on the same samples) of noncorrelation of the maxima:

$$E\left(g=\frac{d_{1.5D}}{d_{2D}}\right)\simeq\frac{\mu_{d1.5D}}{\mu_{d2D}}+\frac{1}{2}\left(\sigma_{d1.5d}^2\frac{\partial^2 g}{\partial d_{1.5D}^2}\bigg|_{\mu_{d1.5D}}+\sigma_{d2D}^2\frac{\partial^2 g}{\partial d_{2D}^2}\bigg|_{\mu_{d2D}}\right)=$$
$$=\frac{\mu_{d1.5D}}{\mu_{d2D}}+\frac{1}{2}\sigma_{d2D}^2\frac{2\mu_{d1.5D}}{\mu_{d2D}^3}=\frac{\mu_{d1.5D}}{\mu_{d2D}}+V_{d2D}^2\frac{\mu_{d1.5D}}{\mu_{d2D}}=$$
$$=\frac{\mu_{d1.5D}}{\mu_{d2D}}\left(1+V_{d2D}^2\right) \tag{78}$$

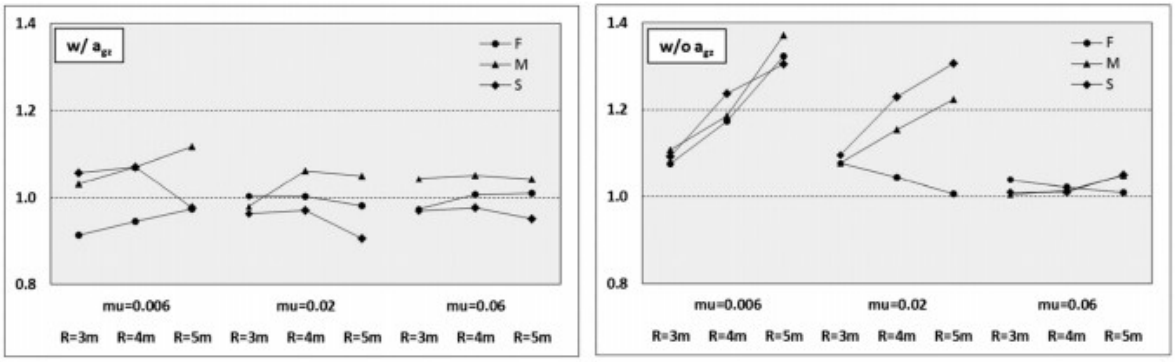

Figure 9. Displacement ratio: 1.5D/2D for the cases (a) with a_{gz} and (b) without a_{gz}.

The first plot, which refers to the case of near-field earthquakes, shows that the 1.5D FP waves around an underestimate of 10% up to an overestimate of 10%. This error tends to reduce as the friction coefficient increases, so that for a friction coefficient equal to 0.06, the results are fairly comparable for all types of soil and for all radii.

The second plot, representative of the case of far-field earthquakes, demonstrates that the 1.5D FP regularly overestimates the maximum displacement. This error tends to increase as the friction coefficient reduces, but still when $\mu_d = 0.02$, the maximum displacement is overestimated by an amount going up to 30% as the radius increases from 3 to 5 m, for soft and medium soil. For high values of the friction coefficient, 0.06 in this study, the results are only slightly overestimated, regardless of the soil type and the radius.

It might be worth noticing that the results of the two case studies, Figures 4 and 7, confirm the outcomes of the parametric analysis summarized in Figure 9, for both cases of near-field and far-field earthquakes.

The aforementioned comparisons, owing to the formulation itself, do not account for possible uplift of the pad. Sarlis and Constantinou [20] propose a valuable description of these effects, but still under uniaxial earthquakes excitation. Given the importance of accounting for this phenomenon, especially for the analysis of near-field earthquakes, the authors intend to develop this topic, starting from the model and formulations proposed in this paper.

These results, along with the remarks about the time-dependent formulation for the stiffness, should be regarded as a first insight of a more comprehensive interpretation of FPs' mechanics to be extended to the analysis of double and triple FPs, so to allow a more accurate and reliable estimate of the stiffness center location.

6 Conclusions

An analytical thermo-mechanics 3D model for FP bearings is proposed. The equations describing the complete motion of a pad on a sphere with friction for the general case of three-directional seismic excitation are derived along with the equation expressing the variation of pad's temperature during the motion. A wide parametric study is conducted, and the comparison between the proposed 2D model and the so-defined ‘1.5D’ model, which resorts to the vector combination of the response of two orthogonal 1D pendulums, is discussed. The study shows that, when higher commonly used vlaues of friction are considered, the 1.5D model currently in use for single-FP isolators predicts displacement demands with an error of 10% or less by comparison with the more accurate 2D model. As friction is reduced for both cases of near-field and far-field earthquakes, the error in predicting the maximum displacement increases, overall leading to an underestimation of as much as 30% in the case of exceptionally low values of friction (e.g., 0.006 in this study). The proposed model also allows deriving a time-dependent formulation for the stiffness, as opposed to the constant value currently assumed. The results of the parametric study prove that the assumption of constant stiffness is not reliable and can lead to a wrong estimate of the stiffness center location in FP-base-isolated structures. Further comparative studies are being developed regarding the temperature variation induced by friction. Finally, extensions of the presented analytical formulation to double and triple FPs are under way.

References

1 Lomax AJ, Michelini A. The use of spherical coordinates in the interpretation of seismograms. *Geophysical Journal* 1988; 93: 405– 412.

2 Zayas VA. Earthquake protective column support, 1987, US Patent 4,644,714.

3 Zayas VA, Low SS, Mahin SA. A simple pendulum technique for achieving seismic isolation. *Earthquake Spectra* 1990; 6: 317– 333.

4 Mokha AS, Navinchandra A, Constantinou MC, Zayas V. Seismic isolation retrofit of large historic buildings. *Journal of Structural Engineering* 1996; 122(3): 298– 308.

5 Minda AA, Gillich G-R, Iavornic CM, Minda PF. Analytical and finite element study for friction pendulum with parameterized sliding surfaces, Proceedings of the World Congress on Engineering, Vol III WCE 2012, July 4–6, 2012, London, UK. 2012.

6 Constantinou M, Mokha A, Reinhorn A. Teflon bearings in base isolation II: modeling. *Journal of Structural Engineering* 1990; 116(2): 455– 474.

7 Mokha A, Constantinou MC, Reinhorn AM. Teflon bearings in base isolation I: testing. *Journal of Structural Engineering* 1990; 116(2): 438– 454.

8 Mokha A, Constantinou MC, Reinhorn AM. Verification of friction model of Teflon bearings under triaxial load. *Journal of Structural Engineering* 1993; 119(1): 240– 261.

9 Wang YP, Chung L-L, Liao W-H. Seismic response analysis of bridges isolated with friction pendulum bearings. *Earthquake Engineering and Structural Dynamics* 1998; 27: 1069– 1093.

10 Tsai CS, Chiang T-C, Chen B-J. Finite element formulations and theoretical study for variable curvature friction pendulum system. *Engineering Structures* 2003; 25(14): 1719– 1730.

11 Almazan JL, De la Llera JC, Inaudi JA. Modeling aspects of structures isolated with the friction pendulum system. *Earthquake Engineering and Structural Dynamics* 1998; 27: 845– 867.

12 Mosqueda G, Whittaker AS, Fenves GL. Characterization and modeling of friction pendulum bearings subjected to multiple components of excitation. *Journal of Structural Engineering, ASCE* 2004; 130: 433– 442.

13 Flom DG, Porile NT. Friction of Teflon sliding on Teflon. *Journal Applied Physics* 1955; 26(9): 1088– 1092.

14 Constantinou MC, Caccese J, Harris HG. Frictional characteristics of Teflon-steel interfaces under dynamic conditions. *Earthquake Engineering and Structural Dynamics* 1987; 16(6): 751– 759.

15 Mostaghel N, Khodaverdian M. Dynamics of resilient-friction base isolator (R-RBI). *Earthquake Engineering and Structural Dynamics* 1987; 15(3): 379– 390.

16 Mokha A, Constantinou MC, Reinhorn AM. Teflon bearings in aseismic base isolation: experimental studies and mathematical modeling. Report No. NCEER-88-0038, National Center for Earthquake Engrg. Res., State Univ. of New York, Buffalo, N.Y., 1988.

17 Constantinou MC, Whittaker AS, Kalpakidis Y, Fenz DM, Warn GP. Performance of seismic isolation hardware under service and seismic loading, Technical Report MCEER-07-0012, 2007.

18 Sarlis AA, Constantinou MC, Reinhorn AM. Shake table testing of triple friction pendulum isolators under extreme conditions, Technical Report MCEER-13-0011, 2013.

19 Kumar M, Whittaker AS, Constantinou MC. Characterizing friction in sliding isolation bearings. *Earthquake Engineering and Structural Dynamics* 2015; 44: 1409– 1425.

20 Sarlis AA, Constantinou MC. Model of triple friction pendulum bearing for general geometric and frictional parameters and for uplift conditions, Technical Report MCEER-13-0010. 2013.

21 Fenz DM, Constantinou MC. Modeling triple friction pendulum bearings for response-history analysis. *Earthquake Spectra* 2008; 24(4): 1011– 1028.

22 Faramarz K, Montazar R. Seismic response of double concave friction pendulum base-isolated structures considering vertical component of earthquake. *Advances in Structural Engineering* 2010; 13(1): 1– 14.

23 Der Kiureghian A, Neuenhofer A. Response spectrum method for multiple support seismic excitations. *International Journal of Earthquake Engineering and Structural Dynamics* 1992; 21: 713– 740.